Nuclear Instruments and Methods in Physics Research A 620 (2010) 182–191

Contents lists available at ScienceDirect

Nuclear Instruments and Methods in Physics Research A

journal homepage: www.elsevier.com/locate/nima

Modeling scintillator and WLS fiber signals for fast Monte Carlo simulations

F.A. Sánchez [a,*], G. Medina-Tanco [b]

[a] Inst. de Tecnologías en Detección y Astropartículas (CNEA, CONICET, UNSAM), Argentina
[b] Inst. de Ciencias Nucleares, Universidad Nacional Autónoma de México, México, D.F., C.P. 04510, Mexico

ARTICLE INFO

Article history:
Received 21 December 2009
Received in revised form
3 March 2010
Accepted 9 March 2010
Available online 18 March 2010

Keywords:
Cosmic rays detectors
Hodoscopes
Plastic scintillator detectors
GEANT4

ABSTRACT

In this work we present a fast, robust and flexible procedure to simulate electronic signals of scintillator units: plastic scintillator material embedded with a wavelength shifter optical fiber coupled to a photo-multiplier tube which, in turn, is plugged to a front-end electronic board. The simple rationale behind the simulation chain allows to adapt the procedure to a broad range of detectors based on that kind of units. We show that, in order to produce realistic results, the simulation parameters can be properly calibrated against laboratory measurements and used thereafter as input of the simulations. Simulated signals of atmospheric background cosmic ray muons are presented and their main features analyzed and validated using actual measured data. Conversely, for any given practical application, the present simulation scheme can be used to find an adequate combination of photo-multiplier tube and optical fiber at the prototyping stage.

1. Introduction

Plastic scintillators (PSC) are widely used in many kinds of radiation detectors. From elementary particle physics to astronomy and astrophysics, they often constitute a basic unit of very complex apparatuses where they play the role of either veto, counting or tracking devices [1–6]. Despite the fact that PSC can be easily shaped to meet almost any detector needs, in many circumstances, the scintillation light produced by charged particles inside the plastic cannot be readily collected at its surface. In such cases, it is a common practice to wrap the scintillator with a highly reflective material and to embed a wavelength shifter (WLS) optical fiber inside the plastic, in order to transport the light from its production site out to the optical sensitive devices responsible for the photon detection. Among the latter, the photo-multiplier tubes (PMTs) are a quite general solution. Once the light is converted into an electronic pulse, and before any subsequent higher level trigger criteria is applied, it is usual to discriminate the analog pulses with front-end electronic boards (FEBs) where the photo sensor devices are plugged. More generally, FEBs are also in charge of amplification and digitalization of the incoming signals.

A wide variety of scintillator detectors have their basic units (BUs) subsystems composed of PSCs, WLS fibers, PMTs, and FEBs as described above. The role of these BUs is to convert the energy deposited in the scintillator material into an electronic signal. Therefore, it is important to have simulation techniques that are able to reliably reproduce that process.

The aim of this work is to present a framework that enables the fast implementation of realistic and robust simulations of the above mentioned BUs.

Sections 2 and 3 describe the general assumptions on which the present simulation scheme relies. Section 4 shows the laboratory measurements needed to properly characterize a particular BU design. The calibration of the remaining free parameters of the simulation is presented in Section 4. The simulation chain thus implemented is used in Section 6 to analyze the response of a simple muon counting rate experiment. General results and conclusions are discussed in Section 7.

2. Simulation technique

As stated earlier, our goal is to convert the energy deposited E_{dep} in a scintillator, into an electronic signal $V^{tot}(x, t)$, taking into account all relevant physical processes (i.e., the scintillation photon yield, the photon transport and reflection inside the plastic, the light absorption, re-emission, and attenuation within the WLS fiber, and the quantum efficiency of the PMT cathode) required in order to reproduce realistically the voltage signal of a general PMT.

The total PMT signal depends on the actual number of photo-electrons extracted from the photo-cathode by the scintillation light and their time distribution. The total number of photo-electrons $n_{phe}(x)$ depends, in turn, on both the distance x from the PMT window at which the light was produced and on the energy deposited inside the scintillator by the impinging particle. Indeed,

* Corresponding author. Tel.: +54 1167727629.
E-mail addresses: fsanchez@cnea.gov.ar, sanchez.f.a@gmail.com (F.A. Sánchez).

0168-9002/$ - see front matter © 2010 Elsevier B.V. All rights reserved.
doi:10.1016/j.nima.2010.03.110

one can write

$$n_{phe}(x) = k(x)E_{dep} \quad (1)$$

where $k(x)$ is a proportionality constant that accounts for the several physical processes we are considering. Given $n_{phe}(x)$, the PMT signal is constructed by adding up the contribution of each photo-electron

$$V^{tot}(x,t) = \sum_{i=1}^{n_{phe}(x)} \upsilon(t-t_i). \quad (2)$$

Therefore, the conversion of the energy deposited into the scintillator into voltage signal is performed through Eqs. (1) and (2) and depends on the choice of:

- the single photo-electron function $\upsilon(t)$,
- the distribution of the times t_i, and
- the tuning function $k(x)$.[1]

Hence, the reliability of the simulation technique rests on how realistic are the criteria used to deal with each one of the previous topics.

2.1. The single photo-electron function, $\upsilon(t)$

Because of the presence of stabilizing capacitors, we can generally assume that the PMT internal circuit is a $C_1R_1-(R_2C_2)^\alpha$ network, i.e., a single high-pass filter (a differentiator, with time constant $\tau_1 = C_1R_1$) followed by α low-pass filters (integrators with $\tau_2 = C_2R_2$). In the case in which all filters have the same time constant $\tau = \tau_1 = \tau_2$, the output voltage of the PMT can be written as

$$\upsilon(t) = \frac{QR}{\tau\Gamma(1+\alpha)}\left(\frac{t}{\tau}\right)^\alpha e^{-t/\tau} \quad (3)$$

where Q is the characteristic single photo-electron charge, R is the circuit load resistance, and $\Gamma(1+\alpha)$ is the gamma function.

2.2. The distribution of times t_i

The actual instant at which an electron is pulled out from the surface of the photo-cathode by the arriving scintillator light depends on three factors: (a) the de-excitation time of the scintillation molecules after the passage of the charged particle through the plastic, (b) the elapsed time before the decay of the fluor molecules which dope the optical fiber and which are responsible for shifting the light from blue to green and, finally, (c) the delay due to the propagation from the production point, x, to the PMT. Later on, the transit time within the multiplication stages of the PMT, may add an additional delay and time spread.

The scintillation and fiber excitation processes are Poissonian. Therefore, the occurrence of an event consisting in the combination of two serial decays of the excited molecules, is a random variable that is the sum of two independent, exponentially distributed, random times. The probability density function for such events is of the form:

$$p_D(t^{decay}|t) = \frac{e^{-t/t_p} - e^{-t/t_f}}{t_p - t_f} \quad (4)$$

where t_p and t_f are the characteristic decay times for the plastic and the fiber respectively.

[1] The discussion of competing approaches for the evaluation of the energy deposition process inside the scintillator is beyond our scope. E_{dep} is obtained from the Geant4 package and, in the present context, it is a mere input for our simulation chain. See Section 5 for further details.

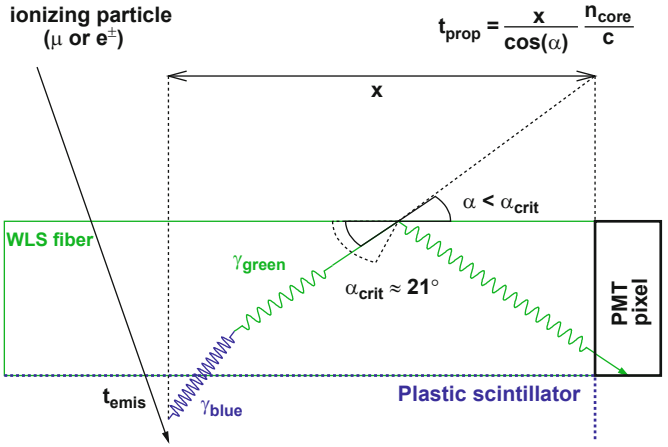

Fig. 1. Assuming the meridional approximation within the fiber, the propagation delay of the green light can be easily estimated as indicated in the figure (any difference in the distance x due to different production points between the blue and green photons is neglected).

On the other hand, assuming the meridional approximation for the green light within the fiber (see Fig. 1), the propagation delay is

$$t^{prop} = \frac{x}{\cos\phi} \times \frac{n_{core}}{c} \quad (5)$$

where the angle ϕ is uniformly distributed due to the isotropic nature of the emission process.

Since the gain is of the order 10^7, the multiplication of one photo-electron through the PMT dynodes involves a large number of electrons. Consequently, the transit times, t^{TT}, can be assumed to follow a Gaussian distribution. The typical time spread in modern PMTs is a few ns [7].

Therefore, under the previous assumptions, for each produced photo-electron contributing to Eq. (2), we consider

$$t_i = t_i^{decay} + t_i^{prop} + t_i^{TT}. \quad (6)$$

2.3. The tuning parameter $k(x)$

Several factors are included in the function $k(x)$: the photon yield of the scintillator, the absorption probability of the produced photons in the bulk of the plastic, the reflection probability off the scintillator walls, the probability of hitting the fiber and of later re-emission within the proper acceptance cone for further propagation, the quantum efficiency of the PMT and, finally, the attenuation of the light along the fiber from the production point to the photo-cathode. In contrast to the former issues, the attenuation can be easily characterized from simple laboratory measurements and, therefore, we can factorize $k(x)$ in the following form:

$$k(x) = k_{Sim}A_{tt}(x) \quad (7)$$

where k_{Sim} does not depend on the distance x and $A_{tt}(x)$ is the attenuation function.

The parameter k_{Sim} is the key factor in the construction of the current simulation scheme. k_{Sim} acts as a tuning parameter which can be adjusted to match real data, simplifying and speeding up the simulation of, many times, poorly known (or difficult to characterize) processes. In any case, it is valuable to be able to make at least a first order estimate of its expected value.

Charged particles crossing the scintillator leave a wake of excited molecules from which blue photons will be radiated isotropically. If we assume that the photon yield is $Y_{ield} \sim 1.25 \times 10^4$ photons/MeV,

which is a typical value for organic plastic scintillators, then we roughly expect that

$$k_{Sim} = Y_{ield} \times p_H \times p_R \times p_Q \tag{8}$$

where p_H is the probability of a blue photon to hit the WLS fiber, p_R is the probability of a green photon to propagate within the fiber by total internal reflection, and p_Q is the quantum efficiency of the photo-cathode.

Most PMTs have a quantum efficiency distribution which reaches $\sim 30\%$ at its maximum. When integrating over all possible wavelengths, this value is lowered. Conservatively, despite the specific spectral response of the cathode, we can assume $p_Q \approx 10\%$.

The transmission probability, p_R, can be easily estimated if we assume a meridional propagation approximation. In this case,

$$p_R = \frac{\Omega_{acc}}{4\pi} = \frac{\int_0^{2\pi}\int_0^{\phi_{crit}} \mathrm{d}\Omega}{4\pi} = \frac{1}{2}(1-n_{clad}/n_{core}) \tag{9}$$

where Ω_{acc} is the solid angle subtended by the acceptance cone, n_{clad} is the refractive index of the fiber cladding, and n_{clad} is the refractive index of the fiber core. Therefore, if $n_{clad}=1.6$ and $n_{clad}=1.49$ (which are common values in commercial off-the-shelf fibers), we obtain $p_R \approx 3\%$.

Using a Bayesian reasoning, the probability of hitting the fiber given that a blue photon was emitted in the plastic, can be written as

$$p_H = P(Hit|Emi) = \frac{P(Hit)}{P(Hit)+P(\overline{Abs})}$$

where $P(\overline{Abs})$ is the probability of a photon to be not absorbed in the plastic (either, in the bulk volume or in its reflective walls). The bulk absorption probability depends on the self-absorption length, Λ_s, while the absorption in the walls depends on the reflection coefficient, R_s. Therefore, considering at most one reflection,

$$P(\overline{Abs}) = P(\overline{Abs_{bulk}})+P(\overline{Abs_{wall}}) = (1-e^{-(w_s+h_s)/\Lambda_s})+(1-R_s)$$

where w_s and h_s, are the plastic width and height, respectively. On the other hand, if the fiber diameter, d_f, is much smaller than w_s and h_s, we can estimate $P(Hit)$ as d_f/w_s+h_s. Hence, if we consider a scintillator strips such that $w_s+h_s \approx 5$ cm, $\Lambda_s \approx 25$ cm, and $R_s \approx 0.98$, we obtain $p_H \approx 13\%$.

With all the above numbers, we arrive to a crude estimation which gives $k_{Sim} \approx 4.8$ photo-electrons/MeV. In Section 5, we show that this value is in good agreement with the results obtained from the simulation-tuning performed using laboratory measurements.

3. Signal features vs. model parameters

In this section, we analyze the dependence of the output voltage signal $V^{tot}(t, x_0)$ at a fix distance x_0, on α and τ (which are determined by the single photo-electron characteristics of the PMT) on the one hand, and on t_p and t_f (which are properties of the scintillator and the fiber) on the other hand.[2]

3.1. Single photo-electron parameters, α and τ

As previously mentioned, the functional form of Eq. (3) is appropriate for a circuit which can be considered as a network of low and high-pass filters. In this case, choosing $C \sim$ nF and $R \sim \Omega$, the rise and fall time are of the order of a few ns. Furthermore, if the PMT produces a gain $G \sim 10^7$, the anode current per photo-electron charge e^-, is

$$I^{phe} = G \times e^- \times \frac{1}{\tau} \sim 10^7 \times 1.610^{-19}\,\text{Coulomb} \times \frac{1}{\text{ns}} \approx 1.6\,\text{mA}.$$

If the load resistance is a few tens of Ω, then the peak voltage of the single photo-electron pulse will be around 10–20 mV and its charge $Q \sim$ pC. The time required by a pulse, described by Eq. (3), to reach its maximum is $\alpha\tau$ while its width is $\sigma^{phe}(\alpha,\tau) = (1+\alpha)\tau^2$. The actual rise and fall times of the single photo-electron pulse are defined by both τ and α. As an example, the top-left panel of Fig. 2 shows the pulse shape $\upsilon(t)$ for different selections of the parameters τ and α. The corresponding accumulated charges as function of time are shown in the top-right panel of the same figure. It can be seen that both, the rise time $\Delta_{50-10} = t_{50}-t_{10}$ and fall time $\Delta_{90-10} = t_{90}-t_{10}$, increase with increasing τ while the pulse shape gets closer to a Gaussian with increasing values of α. The dependence of Δ_{50-10} and Δ_{90-10} on τ and α are shown in the bottom panels of Fig. 2.

3.2. Scintillator and fiber parameters, t_p and t_f

When the PMT is coupled to the scintillator, many photons are expected to arrive to the photo-cathode per energy deposition event. The total output signal at a given distance, $V^{tot}(t,x_0) \equiv V^{tot}(t)$, is the superposition of $n_{phe}(x_0)$ single photo-electron pulses distributed over time in accordance with the probability given by Eq. (4). The top-left panel of Fig. 3 shows 4 cases of p_D for different realizations of the plastic and fiber decay times. It is straightforward to demonstrate that the mean time of the distribution is $\bar{t} = t_p+t_f$ while its spread is $\sigma_t = t_p^2+t_f^2$. Given a fix number of photo-electrons, i.e., a fix charge or energy deposited in the scintillator by an impinging particle, the values of σ_t and σ^{phe} determine the shape of the total voltage signal $V^{tot}(t)$, such that, the smaller the σ_t/σ^{phe} ratio, the larger the probability of overlapping of single photo electron pulses and, therefore, the larger the probability of having higher amplitude signals. Larger σ_t/σ^{phe} ratios, on the other hand, produce wider output signals. The dependence of σ_t on the fiber and scintillation decay times is shown in the top-right panel of Fig. 3.

As an example, we show a random realization of the resulting train of single photo-electron pulses for the particular case of $n_{phe}=6$, $\alpha=4$, $\tau=0.5$ ns, $t_p=1$ ns and $t_f=6$ ns in the top-right panel of Fig. 3. The times required to reach 10%, 50% and 90% of the total charge are also indicated in the figure by vertical lines. It is worth noting that, even if all the above mentioned parameters are kept constant, the total signal is a random variable and, therefore, the outcomes for the rise and fall times (as well as the resulting $V^{tot}(t)$) are different in each realization. The distributions of Δ_{50-10} and Δ_{90-10}, for the previous choice of parameters, are shown in the reduced canvas of the top-right panel of Fig. 3.

It is interesting to note that, even if the mean number of photo-electrons per particle increases (e.g., by doubling the width of the scintillator or by increasing the PMT quantum efficiency) while the remaining parameters are kept constant, the resulting temporal features are almost not affected, as can be appreciated in the bottom-right panel of Fig. 3 (although, clearly, the signal amplitude will be doubled on average).

4. Extracting parameters from laboratory measurements

In this section we discuss the characterization through laboratory measurements of the parameters Q and τ, as well as the function $A_{tt}(x)$, which are essential to perform a realistic signal

[2] We are not interested in this section on the attenuation features which have the unique consequence of reducing the total amount of photo-electrons $n_{phe}(x)$ available for the signal superposition. The attenuation issues will be discussed in the following section.

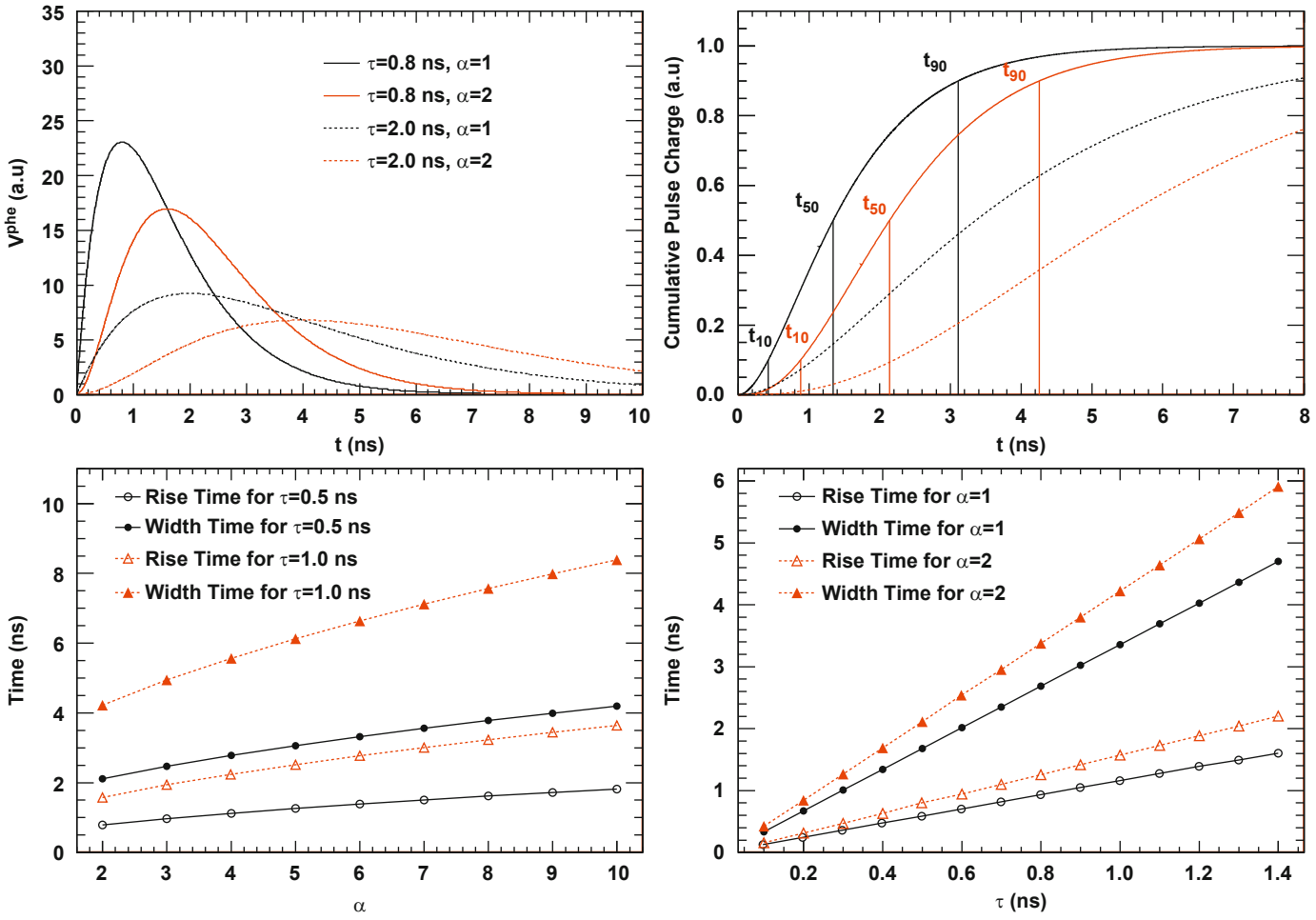

Fig. 2. Single photo-electron simulated features. Different pulse shapes corresponding to different values of τ and α (top-left). Time required to accumulate 10%, 50% and 90% of the total single photo-electron charge (top-right). Dependence of rise time, $t_{50}-t_{10}$, and width time, $t_{90}-t_{10}$, as a function of α (bottom-left) and τ (bottom-right).

simulation. We study a particular case[3]: a $2\,\mathrm{m}\times 4\,\mathrm{cm}\times 1\,\mathrm{cm}$ scintillator strip embedded with a 1.5 cm diameter Bicron BC92 optical fiber, plugged onto a H7546B Hamamatsu multi-anode photo-multiplier. We choose 950 V as reference input high voltage for the PMT, but all the results can be easily scaled to other supply voltages if the PMT gain curve is known. In order to improve the walls reflectivity of the strip, we consider the case of a plastic scintillator wrapped inside a T_iO_2 thin layer.

4.1. Fiber characterization

Light suffers attenuation when propagating along the fiber. The transmission along optical fibers with a core and a cladding of close refractive indexes is well described by a double exponential decay law of the form

$$A_{tt}(x) = a_f e^{-x/\Lambda_{1f}} + (1-a_f)e^{-x/\Lambda_{2f}} \tag{10}$$

where Λ_{1f} and Λ_{2f} are a short and a long effective attenuation length, respectively. The attenuation response given by Eq. (10) can be measured recording the output voltage of a photo-transistor located at one end of the fiber while a light emitting diode (LED) illuminates the fiber at different distances from the photo-transistor. The opposite free edge of the fiber must be black painted in order to avoid reflections which would lead to an overestimation of the attenuation length. The intensity of the light emitted by the LED can be controlled by varying the supplied current and the photo-transistor can be operated in photo voltaic mode. The linearity of the system has to be checked before proceeding to the characterization of the fiber. The LED and fiber emission spectra were also measured. The results of these measurements are shown in the top left and right panels of Fig. 4. It can be seen there that the blue light emitted by the LED (peaked at around 470 nm) is shifted towards longer wavelength when re-emitted by the fiber (peaked at $\sim$525 nm). The result of fitting the light intensity as a function of distance with the decay behavior described by Eq. (10) is shown in the bottom panel of Fig. 4. The obtained fitting parameters are also indicated in the figure. It can be seen that, in the present example, almost 30% of the light is attenuated by the short length ($\Lambda_{1f}\sim 40$ cm) while the longer length (Λ_{2f} is $\sim$6 m) accounts for the remaining 70%.

4.2. PMT single photo-electron features

Essential to the simulation approach presented in this work, are the single photo-electron features of the PMT actually used in

[3] Despite being a particular example, it is a useful one since many actual detectors use this kind of scintillation units, e.g. Ref. [3].

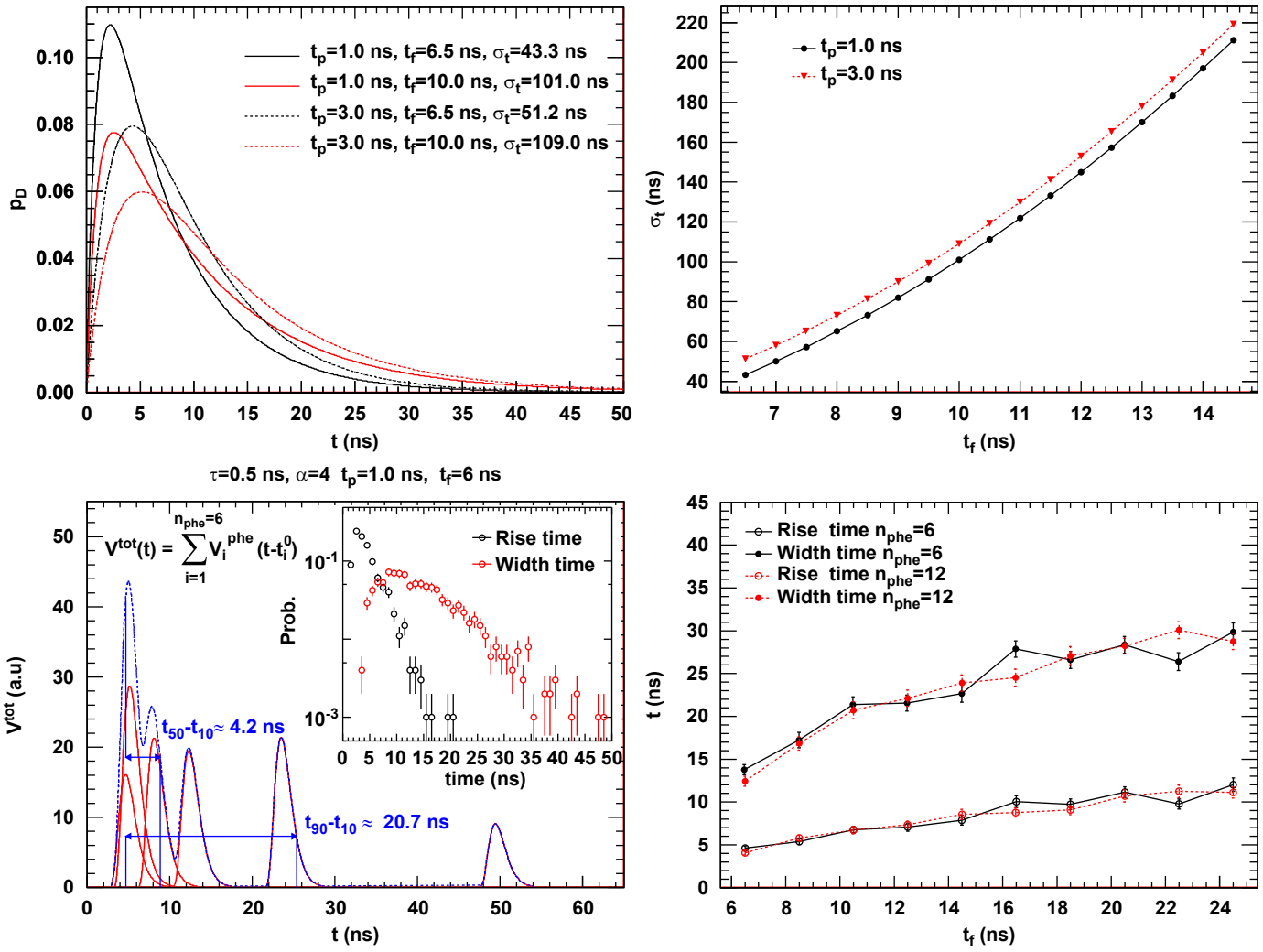

Fig. 3. Muon signal simulated features. Time probability distributions p_D for different scintillation t_p and fiber t_f decay times (top-left). Spread of p_D as a function of t_f (top-right). A random realization of a muon pulse summing the contributions of six single photo-electron pulses (bottom-left). Dependence of rise time, $t_{50}-t_{10}$, and width time, $t_{90}-t_{10}$, as a function of t_f (bottom-right).

the detector to be simulated. Considering a fix α[4] we can see from Eq. (3) that each photo-electron pulse is determined by its charge, Q, and its characteristic time, τ. Therefore, we need to know the distribution functions of these two parameters in order to reproduce signal-to-signal fluctuations adequately and simulate a realistic output signal. These distribution functions were obtained by illuminating the PMT with a LED, at the level of one single photo-electron, and recording the produced signals. As an example, the top left panel of Fig. 5 shows some of those signals, together with the corresponding fits using Eq. (3). It can be appreciated that the selected function adjusts very well the observed signals.

The same procedure was applied for the measurement of the distribution functions of Q and τ for all the 64 channels of a H7546B photo-tube. The results for one PMT anode are shown as an example in the top right and bottom panels of Fig. 5. It can be seen that, after the subtraction of the baseline, the distribution function of Q can be well approximated by a Gaussian, while the distribution function of τ is closer to a Landau. Both approximations can be, therefore, used to fluctuate the single photo-electron pulses during the simulation.

The electronic white noise of the PMT was also measured and parametrized by a Gaussian function.

5. Calibration of free parameters for muon signals

After the determination of the attenuation function $A_{tt}(x)$ and of the appropriate distribution functions for Q and τ, the remaining free parameters of the simulation are k_{Sim}, t_p and t_f. These three latter variables can be calibrated using the atmospheric muon background. To this end, we simulated muons with momentum spectrum following the zenith distribution below

$$I(p_\mu,\theta) = \cos^3(\theta) I_v(p_\mu \cos(\theta)) \tag{11}$$

which reproduces the observed distribution at ground level [8]. The energy deposited in the scintillator strip by the impinging muons, E_{dep}, was calculated using the GEANT4 package [9]. The momenta and angular distribution of the simulated muons are shown in the top left and right panels of Fig. 6 respectively, while the calculated distribution of E_{dep} is shown in the bottom panel of

[4] We took $\alpha = 4$, which adjusted quite well the single photo-electron pulses we measured for our PMT. Nevertheless, it must be noted that α varies from one PMT to another.

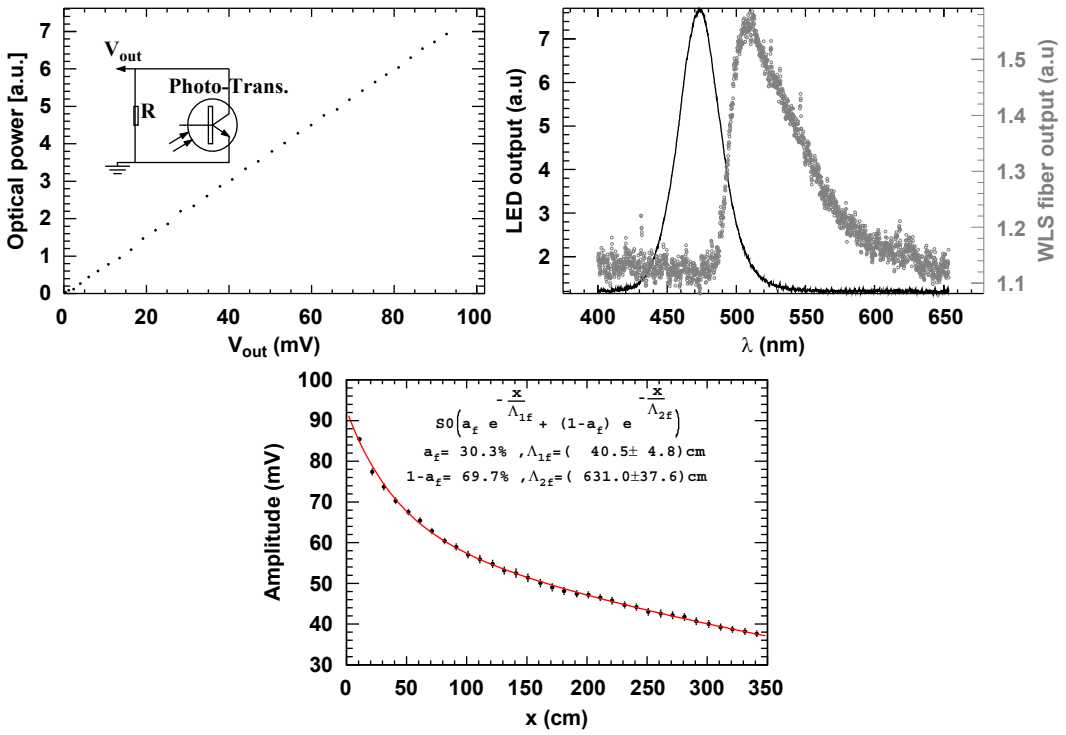

Fig. 4. Characterization of wavelength shifter optical fiber. Experimental system linearity and readout circuit (top left), LED emission and fiber emission spectra (top right), and light attenuation in fiber as function of distance with fit superimposed (bottom).

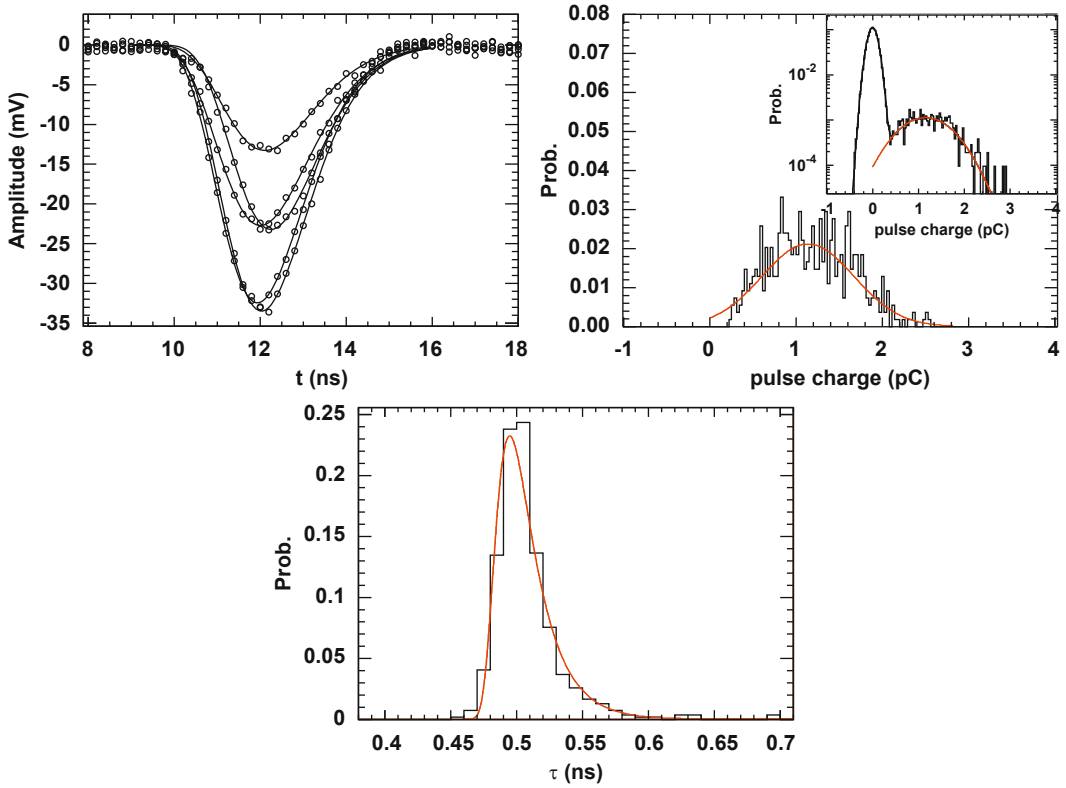

Fig. 5. Laboratory characterization of photo-multiplier tube at 950 V input voltage. Some single photo-electron pulses with their fit superimposed (top left), charge distribution of single photo-electron pulses without (top right large canvas) and with (top right small canvas) baseline noise, and distribution of characteristic time parameter τ (bottom).

the same figure. Clipping corner muons traversing the scintillator strip, are responsible the low energy tail of the E_{dep} distribution in Fig. 6. For each event, the energy deposited by the muon was converted to photo-electrons using Eq. (1). This number was then fluctuated using a Poisson distribution in order to build the electronic PMT response using Eq. (2).

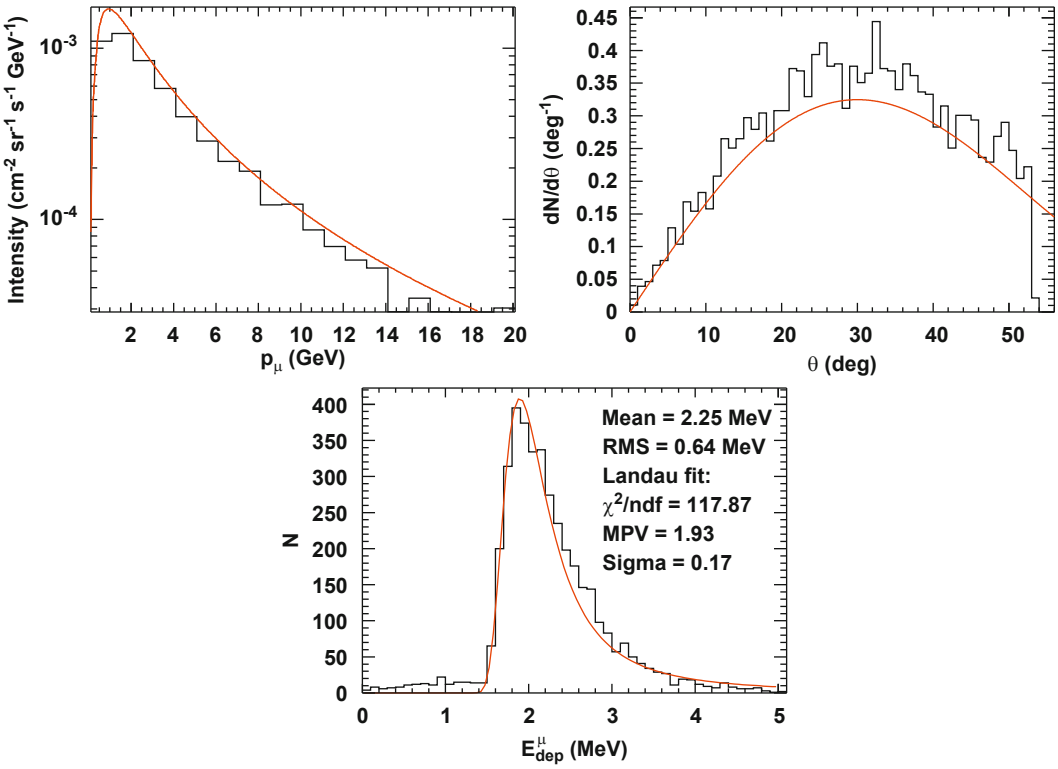

Fig. 6. Input and output of Geant4 simulation. Momenta distribution (top left) and angular distribution (top right) of impinging muons used to trigger the simulation. Energy deposit by the simulated muons in 1 cm thick scintillator plastic with a Landau function fit superimposed (bottom).

The statistical features of signals coming out from the simulation were compared with those of the real signals and the three simulation parameters (k_{Sim}, t_p and t_f) adjusted until a good statistical agreement between simulation output and laboratory measurements was achieved. The experimental setup used to acquire real muon signals is shown schematically in Fig. 7. The selected distance was $x_0=385$ cm[5] corresponding to muons impinging the farthest edge of the scintillator strip. A coincidence in the P1 and P2 detectors triggered the acquisition system.

We found that the time structures of the measured signals can be reasonably matched by the simulations for $t_p=1$ ns and $t_f=6.5$ ns. We also found that, in agreement with our numerical estimate on Section 2.3, around five photo-electrons per energy unit, i.e. that $k_{Sim}\sim 5$ phe/MeV, is the optimum value to reproduce the real charge and amplitude distributions of the measured muon signals. As an example of the good agreement between simulation and real data, Fig. 8 shows two real (right panels) and two simulated (left panels) signals. The rise time Δ_{50-10}, and the width time, Δ_{90-10}, are also indicated in the figures for each pulse. Finally, in Fig. 9, we show that the validation of the whole simulation chain is statistically meaningful. The figure shows the comparison of real versus simulated distributions of charge, amplitude, rise and fall time. It can be see that, for the selected set of parameters, the agreement is very good for all the observables considered.

6. Atmospheric muon rate experiment

The thorough study of the response of a scintillator detector of complex geometry, is beyond the scope of this work. Nevertheless, as a simple example, we will use here the presented simulation strategy to predict the efficiency of a single scintillator strip used as a counting rate device.

We assume a scenario, routinely used in a large variety of experiments, consisting of a PMT attached to a front-end electronic board which discriminates and digitizes the signals at a given sampling rate.[6] Fast FPGA can be used to actually count how many times the outcome signal is above a given discriminator threshold. The schematic channel of such electronic board is shown in the right panel of Fig. 7. Modern FPGA can work at 320 MHz, corresponding to one sample each 3 ns. On the other hand, the resolution of standard discriminators is around 1–2 ns. The double peak resolution t_{dpr} of a counting device as the one we are considering (defined as the time between the leading edges of the two most closely spaced input pulses for which the device is still able to produce two output pulses) is a very important characteristic to have under control during the design phase of the experiment. Because the time structure of the muon pulses (as the double peak shown in Fig. 8), an ideal device (i.e., $t_{dpr}\to 0$) with its threshold set to a low value resolves the multiple peaks of the signals possibly leading to an over-counting of individual muons (if a naive algorithm of counting one muon per threshold crossing is assumed). On the other hand, if the threshold is too high, many signals do not go beyond the threshold and the rate is underestimate. Fig. 10 shows both effects for two particular values of t_{dpr}. It can be seen, that a discriminator with $t_{dpr}\sim 5$ ns would over-count muons by 80% or, in other words, would count nearly two peaks per muon. One way to avoid the over-counting problem is to inhibit the second or subsequent peaks by means

[5] In order to check the independence of the results on the distance, the procedure was later repeated at $x_0=160$ cm. No changes were appreciated.

[6] Despite the fact that many times the signal is also amplified by the FEB, neglecting the amplification phase will not change considerably our results. In fact, fast amplifiers only change the electronic transfer function, broadening a bit the signal but without changing its shape.

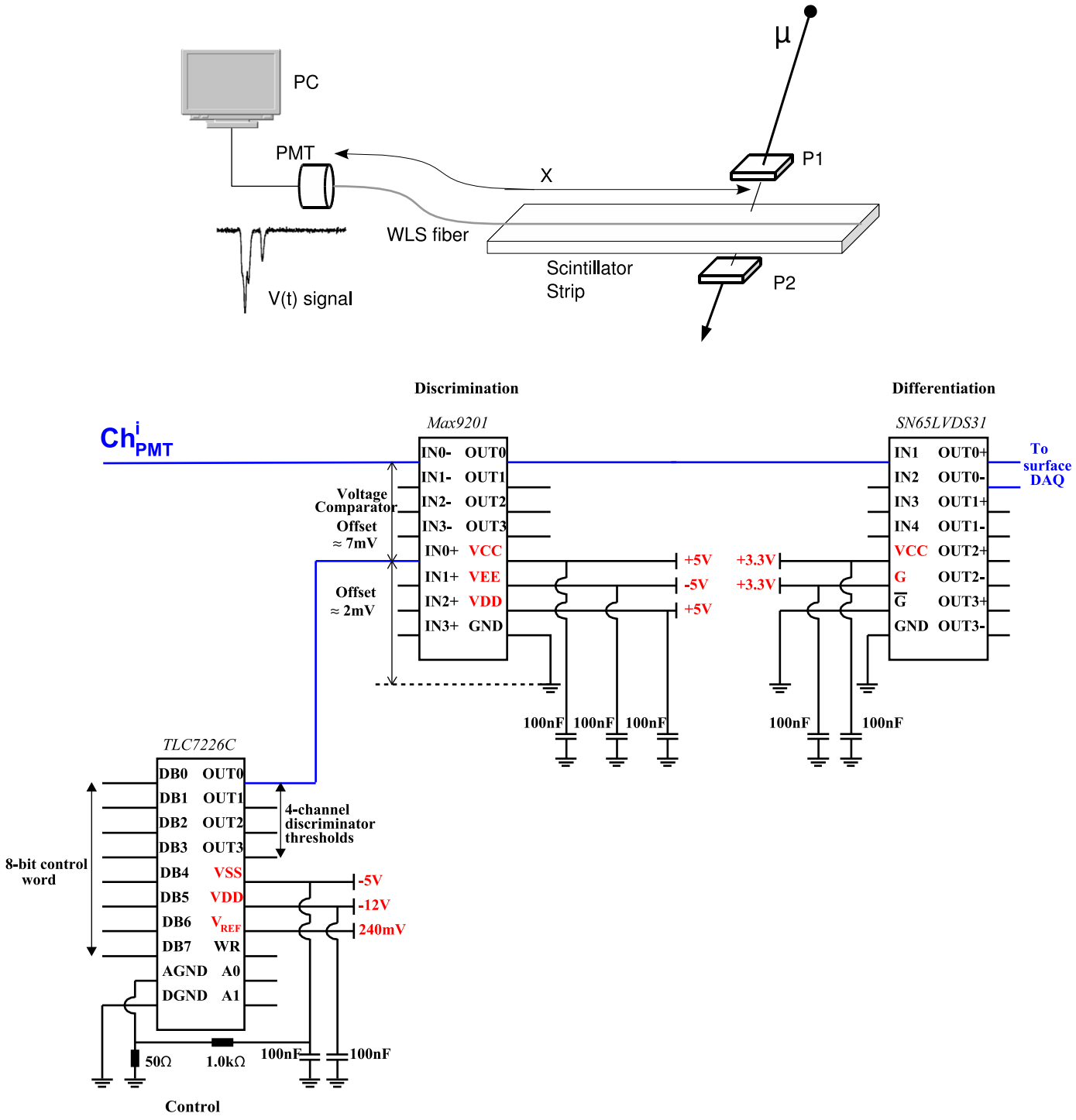

Fig. 7. Experimental setup used to record atmospheric background muons and emulated in the simulation (top). Schematic view of the front-end electronic board used to discriminate muon pulses as function of voltage threshold (bottom).

of a time veto window, t_{veto}. In this way, once a pulse is detected, subsequent pulses are ignored during a time t_{veto}. The best value for t_{veto} depends on the details of detector being designed and on the physics observables to be measured. In our example, we show that a t_{veto} around 50 ns should be enough to eliminate the over-counting for thresholds in the range $\approx 2-20$ mV.

To test our prediction and further validate our simulation, we applied the veto criteria to real muon data. Fig. 10 shows that the agreement between measurements and simulations is very good.

7. Results and conclusion

We present a robust and fast simulation strategy which is able to reproduce, reliably, the response of generic scintillator detectors widely used in particle and cosmic ray physic experiments. The simulation chain starts with the energy deposited by particles inside plastic scintillators and, after taking into account the propagation of light along a wavelength-shifting optical fiber, outputs the corresponding electronic signals produced by a fast PMT. The simulation relies on only three free parameters, and we

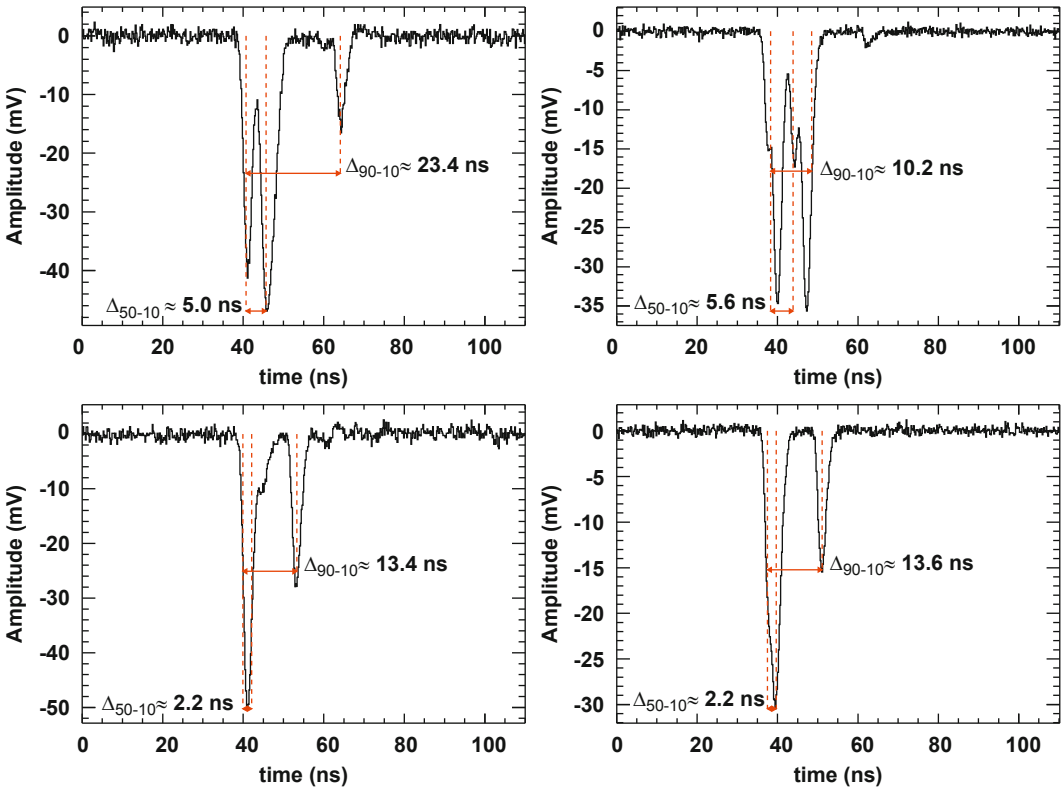

Fig. 8. Real (top and bottom right) and simulated pulses (top and bottom left) of impinging muons at 385 cm from the PMT in an experimental setup as the one indicated in Fig. 7. Dotted vertical lines indicate the times to accumulate 50% and 90% of the total pulse charge.

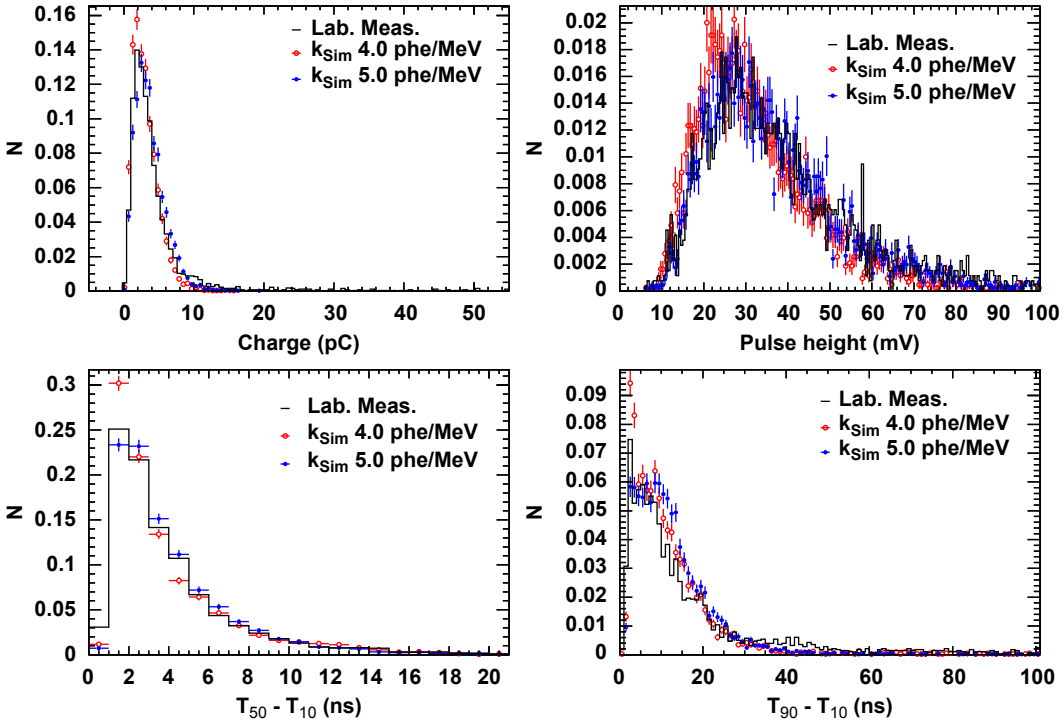

Fig. 9. Real vs. simulated pulse statistics, solid histograms are measurements while full and open circles are simulations with a different value of the k_{Sim} parameter each. The following distribution are displayed: pulse charge (right-top), pulse amplitude (left-top), rise time (left-bottom), and width time (right-bottom).

show how to tune them using laboratory measurements. Thus, the time structure features and statistical properties of the signals are accurately reproduced. We also study the dependence of the output signals on the simulation parameters and demonstrate, in this way, the potential of the presented model as an optimization tool for the design of scintillator detectors. In this later context,

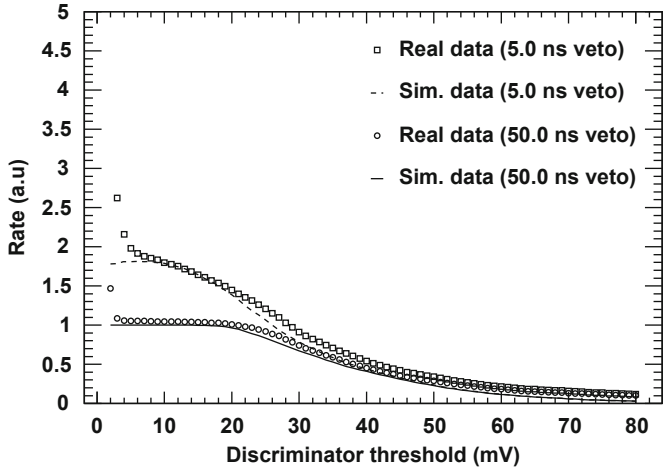

Fig. 10. Muon rate experiment, real vs. simulated results. The counting rate dependence on the veto time as a function of discrimination threshold. Open squares and circles are real measurements while solid and dashed lines are simulations.

the simulation can also aid in the selection of the most adequate components in order to attain specific time, amplitude or charge features of the output signals required by the application in question. Most importantly, the present simulation approach provides a deeper physical understanding of the behavior of a given detector and, due to its modularity and simplicity, it can be replicated and combined in order to reproduce much more complex devices.

References

[1] F. Carminati, et al., J. Phys. G 30 (2004) 1517.
[2] B. Cheynis, et al., Nucl. Instr. and Meth. A 569 (2006) 732.
[3] P. Adamson, et al., Phys. Rev. D 77 (2008) 072002.
[4] A. Etchegoyen, in: 30th International Cosmic Ray Conference, vol. 5, 2008, p. 1191.
[5] F. Sanchez, AIP Conf. Proc. 1116 (2009) 216.
[6] C.P. Achenbach, J.H. Cobb, Nucl. Instr. and Meth. A 539 (2005) 112.
[7] Photonics HAMAMATSU, 〈http://www.hamamatsu.com〉.
[8] D. Reyna, arXiv:hep-ph/0604145.
[9] S. Agostinelli, et al., Nucl. Instr. and Meth. A 506 (2003).